Journal of Energetic Materials
Publication details, including instructions for authors and subscription information:
http://www.informaworld.com/smpp/title~content=t713770432

Modeling High Rate Impact Sensitivity of Perfect RDX and HMX Crystals by ReaxFF Reactive Dynamics

Luzheng Zhang[a]; Sergey V. Zybin[b]; Adri C. T. Van Duin[c]; William A. Goddard III[b]
[a] The Petroleum Recovery Research Center, New Mexico Institute of Mining and Technology, Socorro, New Mexico, USA [b] Materials and Process Simulation Center, Beckman Institute, California Institute of Technology, Pasadena, California, USA [c] Department of Mechanical and Nuclear Engineering, Pennsylvania State University, University Park, Pennsylvania, USA

Online publication date: 15 October 2010

To cite this Article Zhang, Luzheng , Zybin, Sergey V. , Van Duin, Adri C. T. and Goddard III, William A.(2010) 'Modeling High Rate Impact Sensitivity of Perfect RDX and HMX Crystals by ReaxFF Reactive Dynamics', Journal of Energetic Materials, 28: 1, 92 — 127
To link to this Article: DOI: 10.1080/07370652.2010.504682
URL: http://dx.doi.org/10.1080/07370652.2010.504682

Journal of Energetic Materials, 28: 92–127, 2010

ISSN: 0737-0652 print/1545-8822 online
DOI: 10.1080/07370652.2010.504682

Modeling High Rate Impact Sensitivity of Perfect RDX and HMX Crystals by ReaxFF Reactive Dynamics

LUZHENG ZHANG,[1] SERGEY V. ZYBIN,[2] ADRI C. T. VAN DUIN,[3] and WILLIAM A. GODDARD III[2]

[1]The Petroleum Recovery Research Center, New Mexico Institute of Mining and Technology, Socorro, New Mexico, USA
[2]Materials and Process Simulation Center, Beckman Institute, California Institute of Technology, Pasadena, California, USA
[3]Department of Mechanical and Nuclear Engineering, Pennsylvania State University, University Park, Pennsylvania, USA

We report a methodology for rapid assessment of impact sensitivity of energetic materials which uses the ReaxFF reactive force field in reactive dynamics (RD) simulations of the high rate compression/expansion of a perfect energetic crystal. This approach is validated here to study the high rate impact sensitivity of 1,3,5-trinitrohexahydro-s-triazine (RDX) crystal and octahydro-1,3,5,7-tetrazocine (HMX) crystal at different phases (α, β, γ, and δ). These simulations found that for a compression rate of ~8.76 km/s along the [100] direction, RDX crystals at lower volume compression ratios (x = 30, 35, 38%) led only to a

Address correspondence to Sergey V. Zybin, Materials and Process Simulation Center, Beckman Institute, 139-74, California Institute of Technology, Pasadena, CA 91125. E-mail: zybin@wag.caltech.edu

few RDX molecules decomposing and only into primary products. However, at higher compression ratios ($x \geq 40\%$), all RDX molecules in the crystal decompose very quickly, leading to both primary and secondary decomposition reactions, including various intermediates such as NO_2, NO, HONO, and OH and final products such as H_2O, N_2, CO, and CO_2.

For the various phases of HMX, these ReaxFF RD simulations found noticeably higher impact sensitivity for the δ-phase than for other three phases (α, β, and γ). At the same compression ratio $x = 40\%$, all HMX molecules in δ-phase decompose leading to both primary and secondary reaction. However, at 40%, only few HMX molecules in α-, β-, and γ-phases decompose. For a higher compression ratio ($x = 42\%$), increased HMX decomposition is observed for all four phases.

These simulation results for both RDX and HMX crystals agree qualitatively with experiment observations. We also observe a variation of the strain energy in different HMX phases induced by the high rate compression, which could be related to the sensitivity difference of HMX phases. These simulations typically took less than 18 h to run on a single 3.0-GHz processor, demonstrating that the fast compression approach by MD simulations with the ReaxFF force field can be used for a quick evaluation of the sensitivity of energetic materials.

Keywords: computer molecular dynamics, HMX, RDX, sensitivity, shock

Introduction

A detailed description of the chemical reaction mechanisms of condensed energetic materials at high densities and temperatures is essential for understanding events that occur at the reactive front of these materials under combustion or detonation conditions. Under shock conditions, for example, energetic materials undergo rapid heating to a few thousand degrees and are subjected to a compression of hundreds of kilobars, resulting in almost 30% volume reduction. Complex chemical reactions are thus initiated, in turn releasing large amounts of energy to sustain the detonation process [1–3]. Therefore, understanding

the various chemical events at these extreme conditions is essential to build predictive models of material properties that can be incorporated into full continuum approaches of describing the detonation process at the macroscopic level.

Impact sensitivity of energy materials is an important property for the handling of explosive compounds. Determination, evaluation, and prediction of impact sensitivity stimulated numerous studies in the last decades. It has been studied by using various techniques: drop-weight [4], X-ray photoelectron spectra (XPS) [5], molecular dynamics [6], quantum mechanics [7–9], neural networks [10], and others [11–13]. These studies found that the impact sensitivity is influenced by various molecular parameters such as the oxygen balance [14], the molecular electronegativity [15–17], the lengths of the trigger bonds [18–20], and the charge dissymmetry around these bonds in the ground state [21–23] and in excited states [24–27]. However, there is a lack of understanding of the impact sensitivity of energetic materials at the molecular level. Understanding from atomistic simulations will illustrate the detailed chemistry of energetic materials upon impact and reveal the origin of their sensitivity under various conditions.

In order to test/evaluate different energetic materials, we need a quick, but reliable, method to get the information on the impact sensitivity. In this work we used a reactive dynamics (RD) simulation approach equipped with the reactive force field (ReaxFF) to evaluate the sensitivity of pure explosive crystals. The ReaxFF is a reactive force field we developed for numerous reactive systems [28–38]. We have demonstrated that by fitting the ReaxFF parameters to a large, quantum mechanics (QM) derived training set containing energies and geometries for ground state, intermediate, and transition state systems we can obtain a reliable computational method for simulating 1,3,5-trinitrohexahydro-s-triazine (RDX) initiation chemistry [28,29]. Furthermore, we have demonstrated the transferability of the method by developing potentials for, among others, energetic materials [28–33], hydrocarbons [34], silicon and silicon oxides [35], aluminum and aluminum oxides [36], transition metal chemistry [37], and magnesium and magnesium hydrides [38].

In this work, the two similar cyclic nitramines, RDX and octahydro-1,3,5,7-tetrazocine (HMX) were studied by using the ReaxFF to evaluate their impact sensitivities under compressions with different ratios in volume. Both RDX and HMX are energetic ingredients used in various propellants and explosives. Chemical formulas of RDX and HMX are $C_3H_6N_6O_6$ and $C_4H_8N_8O_8$, respectively. The simulations in this study help us to understand the complex physiochemical processes that underlie the detonation of these materials and can lead to methods for modifying the propellant and explosive formulations, which are used to obtain better performance (heat of detonation, detonation velocity) and safety heat, friction or impact sensitivity for different purposes. We demonstrate here that high rate compression/expansion modeling by RD simulations with the ReaxFF can be used for a rapid evaluation of the sensitivity of energetic materials with various formulas and configurations.

Reactive Force Field

The ReaxFF employs instantaneous bond orders, including contributions from σ, π, and $\pi\pi$ bonds, which are calculated from the interatomic distances. These instantaneous bond orders are subsequently corrected with overcoordination and undercoordination terms to force systems toward the proper number of bonds. These bond orders are updated every RD iteration, thus allowing the ReaxFF to recognize new bonds and to break existing bonds. The ReaxFF partitions the overall system energy into contributions from various partial energy terms, as shown in the following:

$$E_{system} = E_{bond} + E_{over} + E_{underd} + E_{val} + E_{pen} + E_{tors} + E_{conj} + E_{vdW} + E_{Coulomb} \quad (1)$$

These partial energies include bond order–dependent terms like bond energies, valence angle, lone pair, conjugation, and torsion angle terms to properly handle the nature of preferred configurations of atomic and resulting molecular orbitals, and

bond order–independent terms that handle nonbonded van der Waals and Coulomb interactions. These latter interactions are calculated between *every* atom pair, irrespective of connectivity, and are shielded to avoid excessive repulsion at short distances. This treatment of nonbonded interactions allows the ReaxFF to describe covalent, ionic, and intermediate materials, thus greatly enhancing its transferability. One important goal in the development of the ReaxFF is to obtain a transferable potential that can not only determine equilibrium bond lengths, valence angles, and torsion angles from the chemical environment of the system but also handle coordination changes associated with reactions. We have been successfully applied the ReaxFF to many systems [28–38]; the parameters used here are the same as those reported earlier for nitramine compounds [28,29]; for a detailed description of the QM test cases included in the development of these parameters, see the supplementary material of Strachan et al. [28]. For a more elaborate description of the ReaxFF partial energy terms see van Duin et al. [34,35].

Simulation Details

To study the shock sensitivity of energetic materials in the condensed phase, we have developed a high strain rate compression/expansion procedure coupled with ReaxFF RD simulations, which mimics the conditions at the detonation front. It consists of four stages illustrated in Fig. 1: (1) a thermally equilibrated, zero-pressure crystal of volume V_0 is compressed uniaxially to $V_0(100-x)\%$ at a constant strain rate u_c during time t_1, where $x = 1 - V/V_0$ is the volume compression ratio (%); (2) perform microcanonical (NVE) RD simulation of compressed crystal for the time $t_2 = 1$ ps; (3) uniaxially expand the crystal along the same direction as in stage (1) to new volume V_0 $(100+x)\%$ during time t_3 at one third of the compression rate, $u_e = (1/3)$ u_c; (4) perform NVE-RD in the expanded cell for the time $t_4 = 4$ ps. We calculated the total simulation time of compression and expansion stages (t_1 and t_3, respectively) using the same compression rate

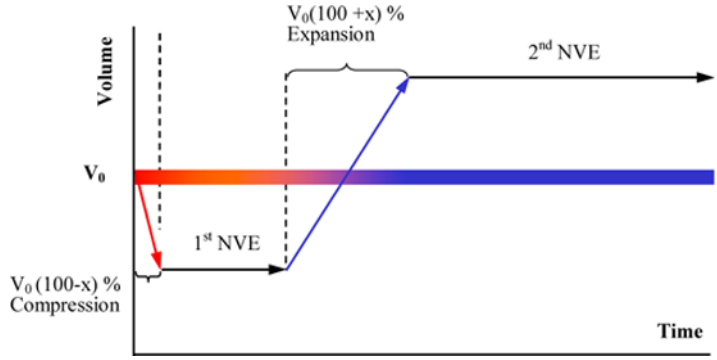

Figure 1. Schematic simulation process of impact sensitivity for a crystal of energetic materials. Apply $V_0(100-x)\%$ uniaxial compression followed by an NVE (1.0 ps); then apply V_0 $(100+x)\%$ uniaxial expansion at the compressed state followed by another NVE (4.0 ps).

$u_c = 8.76$ km/s and the integration time step of 0.1 fs in Table 1. For example, in simulation with the compression ratio of $x = 40\%$ along the [100] direction in RDX crystal, one needs to run 1,290 steps ($t_1 = 0.129$ ps) at the first stage to get $V_0(100-40)\%$ compression and 8,620 steps ($t_3 = 0.862$ ps) at the third stage to reach 140% V_0 expansion.

During the compression and expansion stages, all atom coordinates (but not the velocities) are rescaled at each time step and the periodic boundary conditions are applied in all three dimensions. This procedure was tested on a number of cases and aims to mimic a drop-weight experiment [4]. It should be noted though that the simulated compression rate is substantially higher than the conventional impact loading rate applied to imperfect crystalline materials. At defects and grain boundaries, the temperature may rise significantly under compression, facilitating the formation of hot spots even at quite low strain rates. Besides, the plastic deformation mechanism may differ in various energetic crystals and depend on the strain rate. It was suggested that plasticity in β-HMX may also develop by twinning [39,40] (at least, at the low strain rate

Table 1
Detailed timing (in picoseconds) of the simulation stages of the constant strain rate compression–expansion procedure for different crystals of RDX and HMX at different compression ratios $x = 1 - V/V_0$. The strain rate u_c at compression stage is 8.76 km/s

System	Compression ratio, x (%)	Compression t_1 (ps)	First NVE, t_2 (ps)	Expansion, t_3 (ps)	Second NVE, t_4 (ps)
RDX	30	0.097	1.000	0.647	4.000
	35	0.113	1.000	0.754	4.000
	38	0.123	1.000	0.819	4.000
	40	0.129	1.000	0.862	4.000
	42	0.136	1.000	0.905	4.000
	45	0.145	1.000	0.970	4.000
	50	0.162	1.000	1.078	4.000
α-HMX	40	0.120	1.000	0.800	4.000
	42	0.126	1.000	0.840	4.000
β-HMX	40	0.129	1.000	0.862	4.000
	42	0.136	1.000	0.906	4.000
γ-HMX	40	0.130	1.000	0.878	4.000
	42	0.137	1.000	0.911	4.000
δ-HMX	40	0.155	1.000	1.031	4.000
	42	0.162	1.000	1.083	4.000

loading), whereas RDX has only the plane slipping and fracture mechanisms of deformation.

In this article, we deal with a perfect crystal where no slipping or twinning deformation may occur due to the very small size and periodic boundary constraint. Thus, we need to whack such a crystal really hard to raise the temperature high enough for a rapid decomposition of molecules within tens of picoseconds. We choose the compression rate u_c close to the average velocity of a detonation wave in the simulated materials. Such a constant strain rate technique provides a reasonable agreement

with the results of the piston-driven shock simulations (see section on RDX crystals). However, it might be possible to explore more sophisticated ways of strain rate control, as proposed, for example, in various Hugoniostat techniques [41,42], or simulate nonperfect crystals with defects.

In this work, we use our technique to study the initiation and sensitivity of RDX and four different phases (α, β, γ, and δ) of HMX crystal. The simulations have been performed for six different compression ratios in RDX ($x = 30$, 35, 38, 40, 42, and 45%) and two ratios in HMX ($x = 40$ and 42%) with the same compression rate $u_c = 8.76\,\text{km/s}$ for both RDX and HMX. Because the cell lengths of RDX and various HMX crystal phases are different, the duration of constant rate compression and expansion stages in the simulation procedure will also be different. Detailed simulation times at each stage of the procedure for different crystals and different compression ratios are listed in Table 1.

The packing structures of the RDX and HMX crystals were taken from the Cambridge Structural Database (CSD). Each CSD unit cell was duplicated by $(2 \times 1 \times 1)$ for RDX, $(1 \times 1 \times 2)$ for α-HMX, $(4 \times 1 \times 2)$ for β-HMX, $(2 \times 2 \times 1)$ for γ-HMX, and $(2 \times 2 \times 1)$ for δ-HMX, providing in total of 16 energetic (RDX or HMX) molecules in the RDX, α-HMX, β-HMX, and γ-HMX supercells (the latter also includes 8 additional H_2O molecules) and 24 molecules in the δ-HMX supercell. The uniaxial strain is applied along the X-direction of the CSD cell for RDX, β-HMX, and γ-HMX; along the Y-direction of the α-HMX cell; and along the Z-direction of the δ-HMX cell. Each supercell structure was optimized by energy minimization using the ReaxFF force field,and then equilibrated at $T_0 = 300\,\text{K}$ by performing 5 ps canonical ensemble (NVT)-RD simulation followed by 2.5 ps isothermal-isobaric ensemble (NPT)-RD simulation at the pressure $P = 0$ in order to remove the residual stresses. The temperature of the system was controlled by a Berendsen thermostat [43] with a damping constant of 50 fs. A Berendsen barostat was used in the NPT simulation to change the system volume uniformly in all three directions, resulting in a decrease of the system pressure to about 0.1 GPa (the pressure damping

constant was set to 5,000 fs). The final structures were then used to carry out the previously described four-stage compression–expansion RD simulations with the ReaxFF to study the initial response and the sensitivity of these explosives at different compression ratios.

The integration time step was set to 0.25 fs in the preliminary NVT and NPT simulation and to 0.1 fs in the controlled rate strain RD simulations. These time steps provide good energy conservation with the ReaxFF method. The atom coordinates and the bond orders were recorded in a trajectory file at every 0.20 ps and then used to determine the molecular species in the system. The bond order cutoff for molecule recognition used in the species analysis for all cases was 0.3; note that this cutoff does not affect system energies or forces. The molecule recognition in the species analysis was performed by using the connection table generated at each time step and calculating molecular components and their compositions in the system [34]. The time evolution of the abundance of reactants, products, and intermediates provides detailed information on the chemical reaction pathways inside the energetic crystals under high strain rate conditions of their compression and expansion and elucidates the factors that affect energetic material sensitivity.

Results and Discussions

RDX Crystal

We first tested RDX crystal with the controlled strain procedure using five different uniaxial compression–expansion rates $x = 30$, 35, 38, 40, and 45% along the x-direction of the CSD cell (i.e., [100] direction). Figures 2a–2d display the time evolution of the system temperature, potential energy, total number of fragments per RDX molecule, and the system pressure, respectively. For the lowest compression ratio $x = 30\%$, the system temperature always stays below 1200 K and the number of fragments per RDX molecule remains 1.0 during the simulation process except for a short period at the compression stage. There the number of fragments becomes less than one because

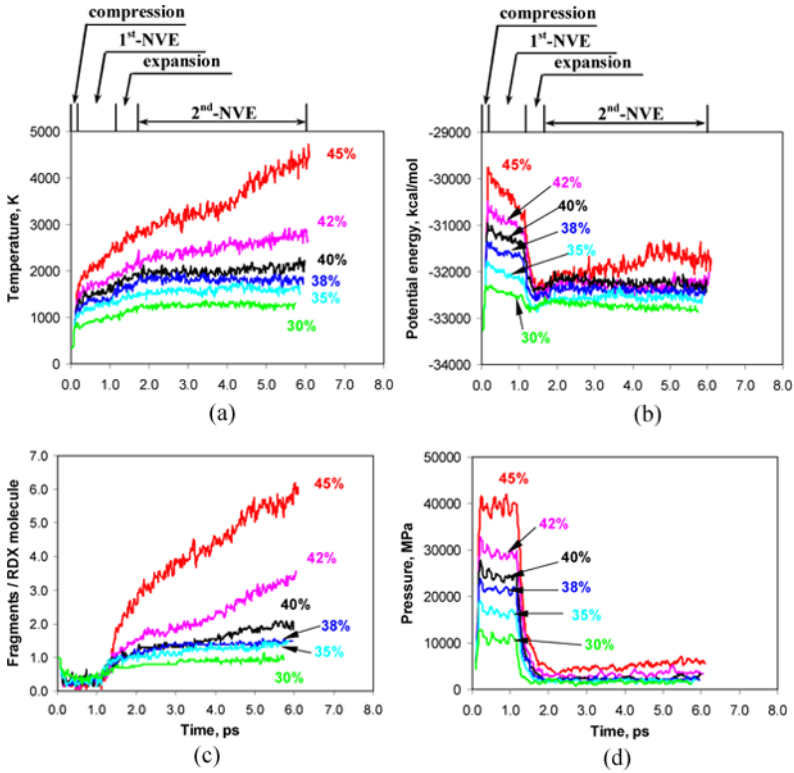

Figure 2. System temperature (a), potential energy (b), fragments (c), and pressure (d) for the RDX crystal in different regions (compression, first NVE, expansion, and second NVE) at the compression ratios of $x = 30$, 35, 38, 40, 42, and 45%.

of the clustering of RDX molecules (some of the molecules are pushed very close to each other under compression and form a cluster that cannot be discriminated by the recognition procedure based on the fixed bond order cutoff criteria). The degree of such clustering increases when the compression ratio grows in the beginning of the first simulation stage (see Fig. 2c). It is *not* related to the chemical reactions in the molecules and will disappear when the system is expanded as seen in Fig. 3a at

$x = 30\%$. For the highest compression ratio $x = 45\%$, the system temperature increases dramatically up to 4520 K (Fig. 2a). Such a sharp increase in temperature is due to the initiation of chemical reactions in the system when chemical bonds in molecules are broken under high pressure and temperature,

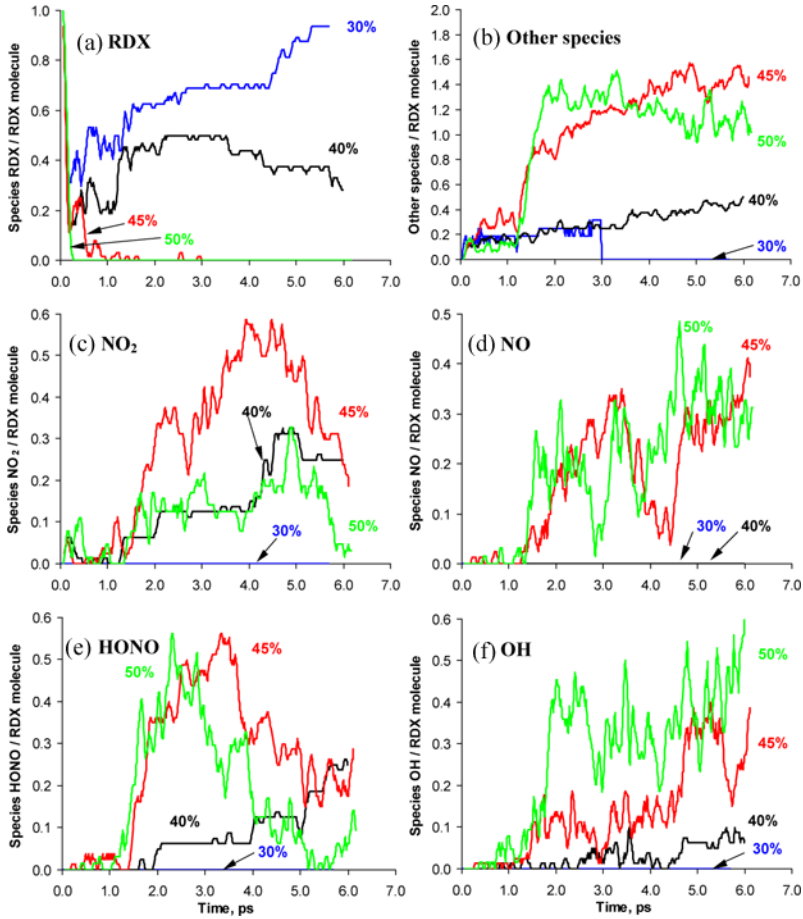

Figure 3. Individual species analysis of (a) RDX, (b) other species (c) NO_2, (d) NO, (e) HONO, and (f) OH for RDX crystal at the compression ratios of $x = 30$, 40, 45, and 50%.

and new products such as H_2O, N_2, CO, and CO_2 are formed providing a positive energy balance from such reactions (e.g., N_2 molecules start to appear after 1.3 ps, resulting in a high energy release). Because of those reactions, the number of fragments per RDX molecule grows to about 3.1 at the end of the expansion and then continuously increases during the NVE stage up to 5.9 in the end.

In order to determine the critical compression ratio at which the explosive RDX gets detonated, we collected the temperature and the number of fragments per RDX molecule at the end of each action (i.e., compression, first NVE, expansion, and second NVE). Figures 4a and 4b show the plots of temperature and number of fragments vs. compression ratio at different stages. At lower compression ratios ($x < 40\%$), the temperature increase across different stages is quite small. Particularly, the temperature has almost no change at the end of expansion and second NVE stages, which also correlates with a small change in the fragments (Fig. 4b). The temperature and fragments, however, increase substantially when the compression ratio is larger than 40%. For instance, the final temperatures are 2790 and 4520 K and the fragments per RDX molecule are 3.6 and 5.9 for $x = 42$ and 45%, respectively. Our simulation results suggest that the critical compression ratio is around $x = 40\%$ for RDX at the simulated compression rate of 8.76 km/s.

The behavior of the system potential energy provides further evidence of an existence of the compression threshold for the initiation of decomposition. At the compression stage (<0.15 ps) the potential energy per RDX molecule increases by 52.1, 70.2, 104.3, 116.6, 137.8, and 172.4 kcal/mol for compressions of $x = 30$, 35, 38, 40, 42, and 45%, respectively (see also Fig. 2b). The details of potential energy change at each simulation stage are given in Fig. 5. The largest change is observed at the expansion and second NVE stage for the compression ratio $x = 45\%$.

We also compared the evolution of system pressure during the simulations, which is plotted in Fig. 2d and exhibits the maximum at the compression stage. It attains about 13 GPa for the lowest compression ratio $x = 30\%$, and it rises up to about

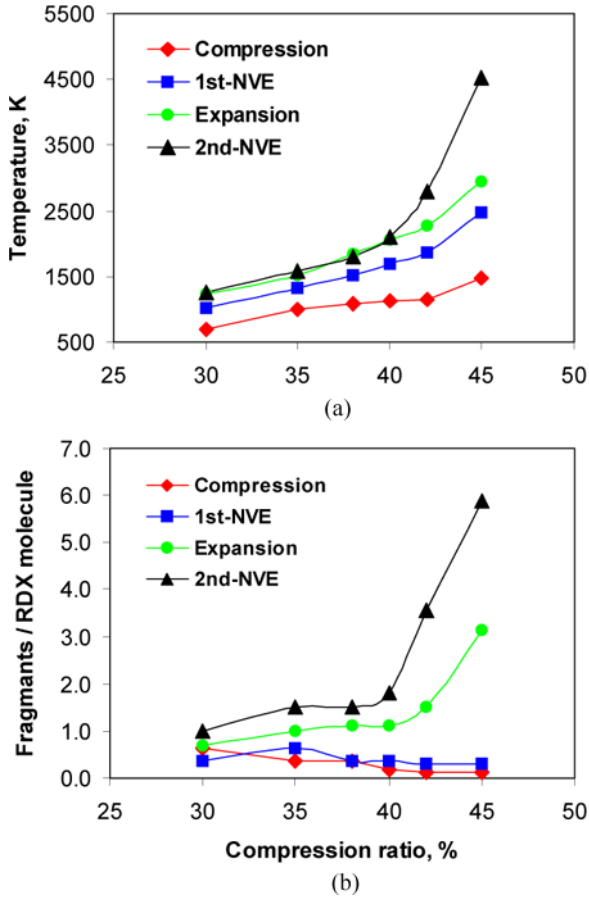

Figure 4. (a) Temperature and (b) fragments vs. compression ratio for the RDX crystal in different regions: compression, first NVE, expansion, and second NVE.

45.5 GPa for the highest ratio $x = 45\%$, overshooting the experimental value of the RDX detonation pressure [1]. For the threshold compression $x = 40\%$, the pressure at the end of compression stage remains about 30.2 GPa, which is still slightly below the detonation pressure. Correspondingly, we observed only small

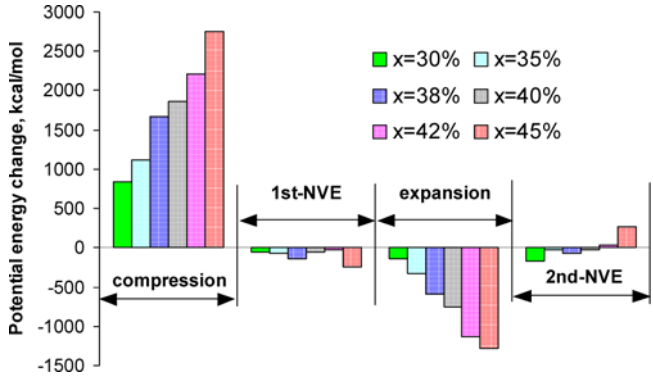

Figure 5. Potential energy change in different regions for RDX crystal under compression ratios $x = 30$, 35, 38, 40, 42, and 45%.

reactions during the expansion for $x = 40\%$ with a slow increase of the fragments up to 1.8 during the rest of simulations. The pressures at the end of the compression stage are plotted in Fig. 6a. For a comparison, Fig. 6b also shows the average pressure at the end of the second NVE simulation. At low compression ratios ($x < 40\%$), almost no reaction is found in the system, resulting in a very small pressure increase at the end of the simulation. However, for higher compressions ($x > 40\%$), the induced pressure becomes higher than the detonation one, and all molecules are decomposed very quickly with many primary and secondary reactions, considerably elevating the final system pressure up to 4.4 and 6.4 GPa for $x = 42$ and 45%, respectively. It also indicates a critical change in the response of RDX crystal above the compression threshold $x = 40\%$.

In order to visualize the resulting fragments of each system, we display the initial and final configuration from each simulation in Figs. 7a–7d. The degree of decomposition of RDX molecules is very different: there is almost no decomposition for $x = 30\%$, whereas every molecule is decomposed at $x = 45\%$. For the case of $x = 40\%$, we can see more reacted molecules, but the degree of decomposition remains much less than in the case of $x = 45\%$.

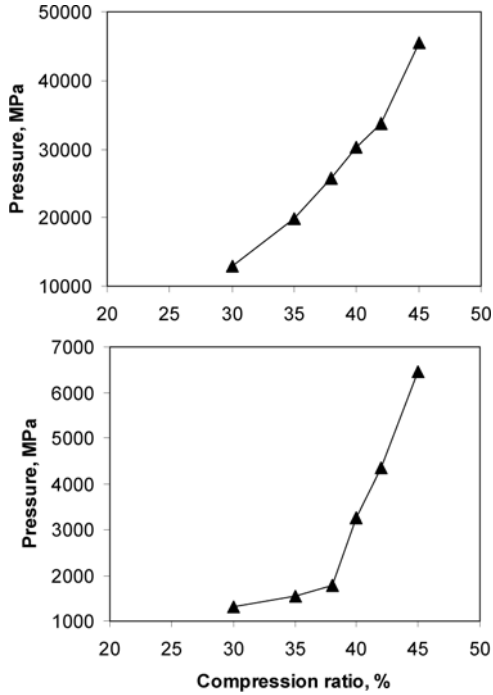

Figure 6. (a) Maximum pressure under compression and (b) final pressure for the RDX at $x = 30$, 35, 38, 40, 42, and 45%.

The analysis of evolution of the system temperature, potential energy, number of fragments per molecule (degree of decomposition), and the system pressure leads to a consistent conclusion. It suggests that in the controlled strain RD simulation of RDX crystal at the compression rate of 8.76 km/s, the critical compression threshold for initiation of decomposition on a very short (picosecond) timescale is about $x = 40\%$. Within the simulation time ($\sim$6 ps) we have not observed the decomposition of RDX molecules in a crystal compressed below this critical value. On the other hand, RDX molecules start to decompose at compression $x = 42\%$ and above, with a fast increase in the products of chemical reactions and the degree of decomposition.

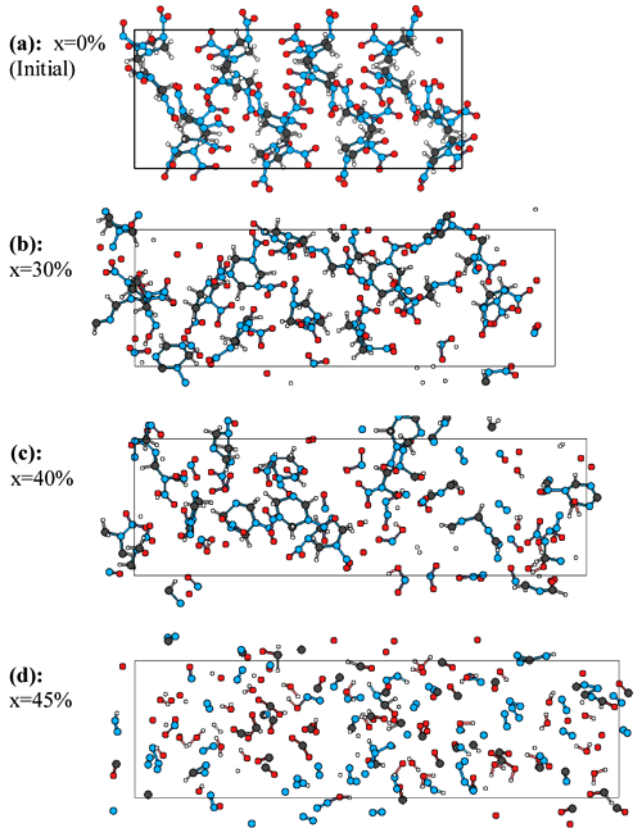

Figure 7. Snapshots of the last frame for the RDX crystal at different compression ratios $x = 0$, (b) $x = 30\%$, (c) $x = 40\%$, and (d) $x = 45\%$.

To test the reproducibility of these impact sensitivity simulations by the procedure coupled with RD simulations proposed in this work, we repeat nine simulations on RDX crystal with the highest compression ($x = 50\%$) using the same compression rate but varying initial atom velocities in the starting configuration. Figures 8a–8c give the system properties—temperature, potential energy, the number of fragments per RDX molecule, and system pressure—for all nine simulation cases,

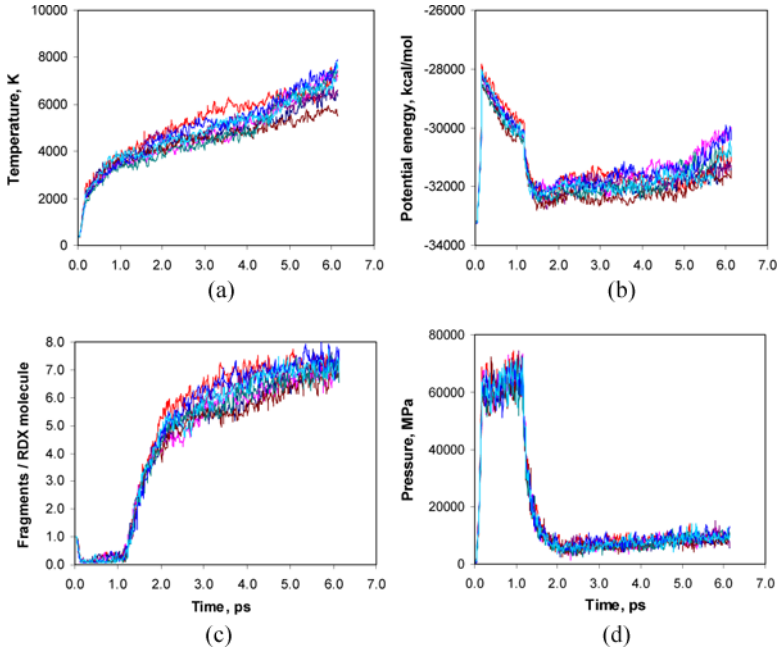

Figure 8. System temperature (a), potential energy (b), fragments per RDX molecule (c), and pressure (d) for the RDX crystal at the compression ratio of $x = 50\%$ from multiple runs. Reproducible data can be obtained for the fast compression simulations.

respectively. These plots show that simulation results are indeed reproducible.

Figure 2c only shows the total number of species in the system during simulations. To identify detailed species in each case, we performed species analysis on the simulation data and retrieved the number of individual species generated by chemical reactions occurring in the RDX crystal. As an example, Fig. 9 gives a detailed species analysis for major components and intermediates in the RDX system at the compression ratios of $x = 42$ and 45%. Because fewer new species are generated at the lower compression ratios $x = 30$, 35, 38, and 40%, it is not necessary to do a detailed species analysis for

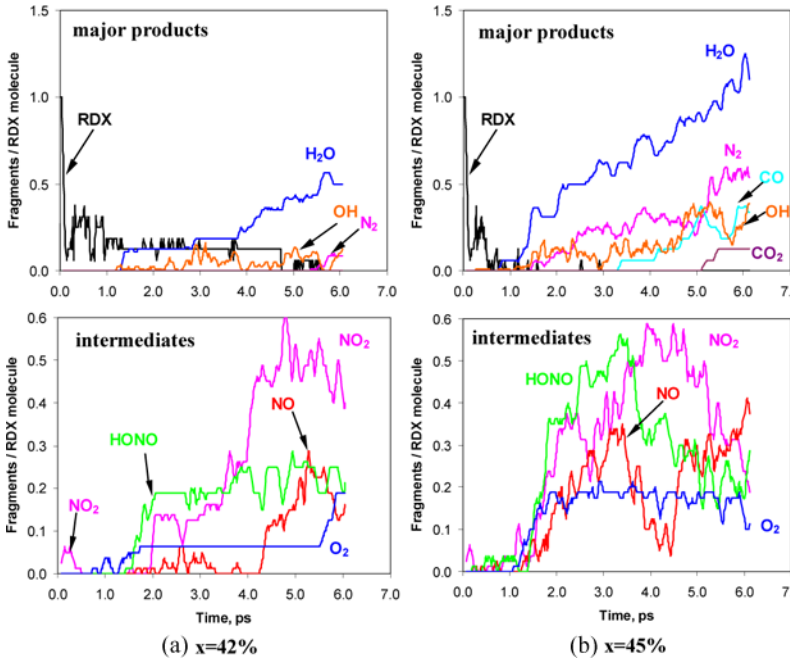

Figure 9. A detail species analysis for the RDX crystal at the compression ratios of (a) $x = 42\%$ and (b) $x = 45\%$.

these cases. For clarity, only those components that have higher maximum concentration than 1 are shown in this figure. The species analysis shows that all RDX molecules decompose very quickly at $x = 42$ and $x = 45\%$ and that components such as NO_2, NO, HONO, CO, CO_2, H_2O, N_2, OH, and O_2 are identified from the simulation, which is in qualitative agreement with experimental results [39]. This detailed species analysis also shows the trend of how these components are changed with the compression ratio. As shown in Fig. 9, products N_2 and H_2O are much more dominant at $x = 45\%$ than at $x = 42\%$ and the first formation time of N_2 at $x = 45\%$ ($t = 0.8$ ps) is much earlier than that at $x = 42\%$ ($t = 5.3$ ps). Moreover, new products CO and CO_2 are observed in the system with compression ratio $x = 45\%$, whereas no CO and CO_2 are found at $x = 42\%$. It is

also found that the intermediates such as HONO and NO_2 and NO at $x = 45\%$ are much more prevalent than at $x = 42\%$. The species analysis provides clear evidence that more chemical reactions are involved in the system when a higher compression ratio is applied to the RDX crystal.

As discussed above, the RDX crystal at $x = 40\%$ compression is about to reach the detonation point and part of the RDX molecules just begin to decompose (primary reactions). However, for the cases with $x > 40\%$, the RDX crystal is fully initiated and the decomposition of RDX molecules includes not only primary reactions but also secondary reactions, which form final exothermic products like H_2O, N_2, CO, and CO_2 observed frequently in experiments [44,45]. This information on individual species can provide hints as to how RDX molecules dissociate under higher compression ratios. Figures 3a–3f compare each individual fragment per RDX molecule at different compression ratios. We include the case at very high compression ratio 50%, so that we can show the evidence of secondary reactions in such a system. Four compression ratios $x = 30$, 40, 45, and 50% are compared in this figure. The individual fragments include RDX, NO_2, NO, HONO, OH, and others, which constitute a sum of the fragments whose number is never greater than 1 at any period within the simulation window. At the low compression ratio $x = 30\%$, there is no chemical reaction at all, so all RDX molecules are kept in the system after the simulation is done. At higher compression ratios, however, most RDX molecules decompose: some RDX molecules are left for $x = 40\%$, but there are no RDX molecules left in the cases for $x = 45$ and 50% (Fig. 3a). The degree of decomposition for the cases at $x = 45$ and 50% are much higher than that for $x = 40\%$ and thus more intermediates NO_2 and NO are produced (see Figs. 3c–3d). The number of the intermediate HONO for the cases of $x = 45$ and 50% for early times (<2.0 ps) is more than that for the case of $x = 40\%$. But it dramatically decreases after 3.0 ps for $x = 45$ and 50% and increases for $x = 40\%$ (Fig. 3e). This is because the secondary reactions occur for the cases of $x = 45$ and 50% after 3.0 ps and HONO molecules react with other intermediates to form

final products such as N_2 and H_2O. These simulation results provide further evidence that both primary reactions and secondary reactions occur for the cases at compression ratios higher than the critical point at which the RDX crystal is detonated.

To verify the predictions obtained with the proposed constant strain rate compression–expansion procedure, in Fig. 10 we provide the results of our previous RD simulations of piston-driven shock compression in the RDX crystal containing 128 molecules. The crystal is compressed by a piston moving along the [100] direction at constant velocity $u_p = 4\,\text{km/s}$, reaching the peak compression ratio of about 44% at the time of 0.8 ps and then bouncing back. Because the crystal has an

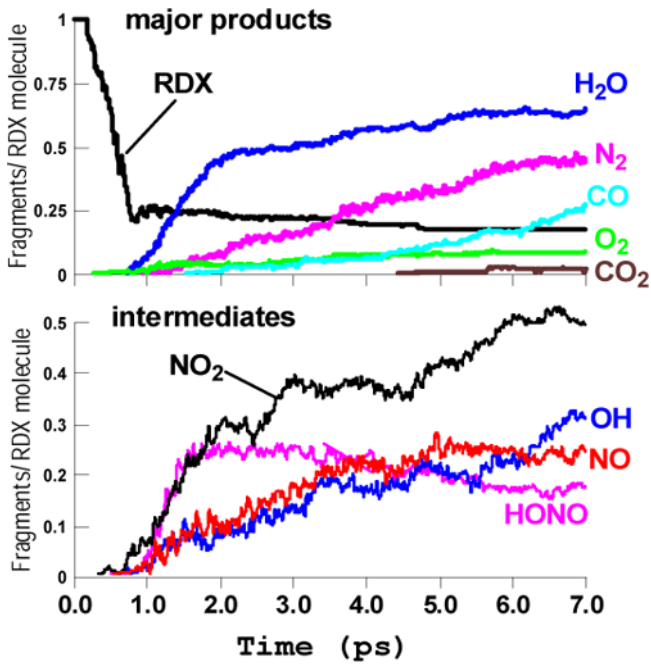

Figure 10. Product frequencies per molecule for the piston-driven shock compression of RDX crystal with 128 RDX molecules at piston velocity $u_p = 4\,\text{km/s}$.

open surface on the opposite side, there is no limit for the volume expansion in contrast to the controlled strain procedure. In particular, some of the surface RDX molecules are pushed away by the emerging shock wave and remain undissociated. Still, the final product distribution of piston-driven shock and controlled strain simulations at the compression ratio $x = 45\%$ are in quite reasonable agreement, indicating that the proposed procedure can be helpful in testing the sensitivity of energetic materials under high strain rate compression.

HMX Crystals in Different Phases

From the simulations on RDX described in the previous section, we have found that the critical compression ratio for this nitramine compound is about 40%. In order to test the sensitivity of HMX in different phases, similar RD simulations were performed on HMX crystals for four phases (α-HMX, β-HMX, γ-HMX, and δ-HMX) with compression ratios $x = 40$ and 42%. Figures 11a and 11b show the system temperature, number of fragments per HMX molecule, and average pressure when compression ratios $x = 40$ and 42% are applied to these four phases of HMX crystals, respectively. The highest temperatures are 1643, 1728, 1646, and 2936 K at $x = 40\%$ and 2404, 1755, 1772, and 3625 K at $x = 42\%$ for α-HMX, β-HMX, γ-HMX, and δ-HMX, respectively. The number of fragments per HMX molecule are 1.4, 1.6, 1.8, and 4.5 at $x = 40\%$ and 3.3, 1.4, 2.2, and 6.0 at $x = 42\%$ for these four phases. Clearly, δ-HMX is the most sensitive and β-HMX is the most stable among the four phases. The pictures (middle row in Fig. 11) show that during the compression regime the HMX molecules of every phase cluster together and partially decluster back into HMX molecules during expansion (see Fig. 12a and related discussion), as observed in the RDX crystal mentioned in the previous section. For a visual illustration, Figs. 13a–13d display system configurations at the end of the simulations were finished for the four HMX systems. These system configurations confirm that the highest degree of decomposition can be found in δ-HMX.

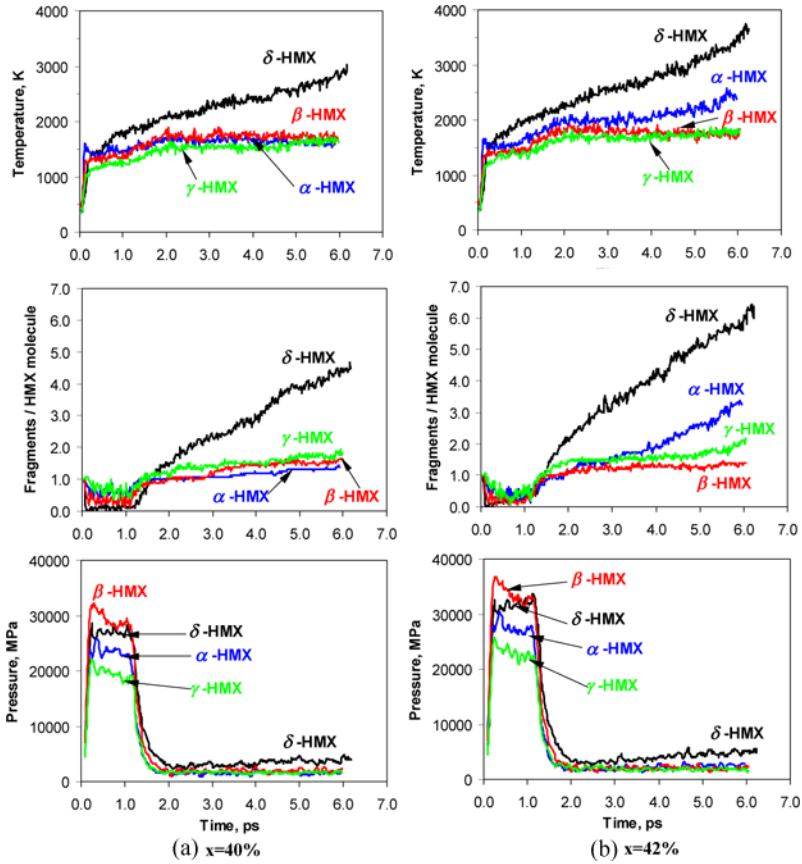

Figure 11. System temperature, fragments per HMX molecule, and pressure for α-HMX (blue lines), β-HMX (red lines), γ-HMX (green lines), and δ-HMX (black lines) at the compression ratios of (a) $x = 40\%$ and (b) $x = 42\%$.

The system pressures during simulations for each case are plotted in Fig. 11 (lower row). The pressure after compression reaches 26.4, 35.4, 21.7, and 31.9 GPa at $x = 40\%$ for α-HMX, β-HMX, γ-HMX, and δ-HMX, respectively. These pressures increase from 1 up to 6 GPa when the compression ratio is changed from 40 to 42%. The system pressure of β-HMX is less than

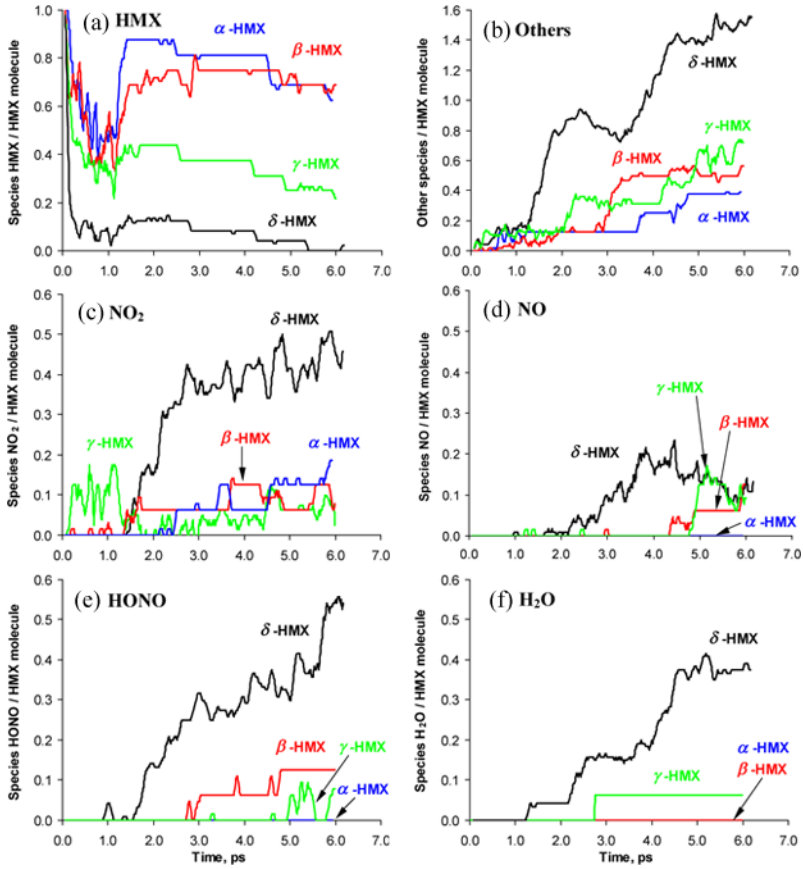

Figure 12. Individual species analysis of (a) HMX, (b) HONO, (c) NO_2, and (d) NO for α-HMX (blue lines), β-HMX (red lines), γ-HMX (green lines), and δ-HMX (black lines) at the compression ratio of $x = 40\%$.

experimental detonation pressure (39.2 GPa) [1,46,47] and almost no HMX molecules are found to decompose in the β-phase. This shows that the β-HMX crystal is the most stable among these four phases. Because HMX molecules in the δ-phase decompose very quickly and many product molecules are generated during the decomposition, the final pressure of

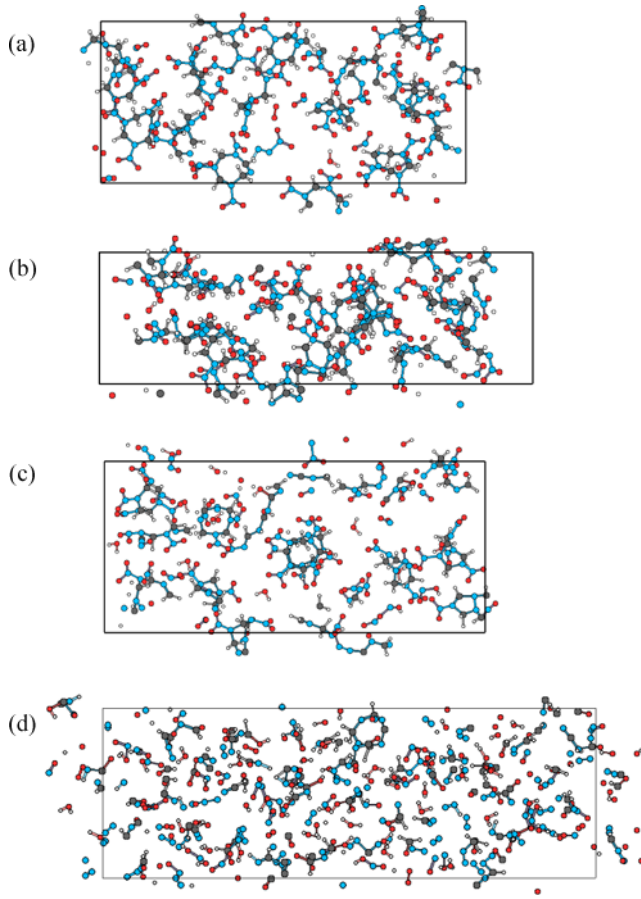

Figure 13. Snapshots of the last frame for the HMX crystals at $x = 40\%$ compression ratio: (a) α-HMX, (b) β-HMX, (c) γ-HMX, and (d) δ-HMX. The highest degree of decomposition of HMX molecules is observed in the δ-phase.

the δ-phase is about 4.8 GPa at $x = 40\%$ and 6.4 Gpa at $x = 42\%$, which is larger than those of the α-, β-, and γ-phases (1.8 Gpa at $x = 40\%$ and 2.4 Gpa at $x = 42\%$).

To determine the order of the sensitivity of HMX in these four phases, we collected the system temperatures and

fragments per HMX molecules in the region of compression, first NVE, expansion, and second NVE. Figures 14 and 15 give the temperatures and number of fragments at the end of each action for the HMX crystals at $x = 40$ and 42%. Both temperature and the number of fragments from δ-HMX increase much faster from one region to another than those from α-HMX, β-HMX, and γ-HMX. Particularly, this increase becomes much more prominent at a higher compression ratio of 42%. With this high compression ratio, the difference between the α-phase and the β-phase is distinguished; that is, α-HMX is more sensitive than β-HMX. For γ-HMX, it is easy to tell that at lower compression ratio $x = 40\%$ it is more stable

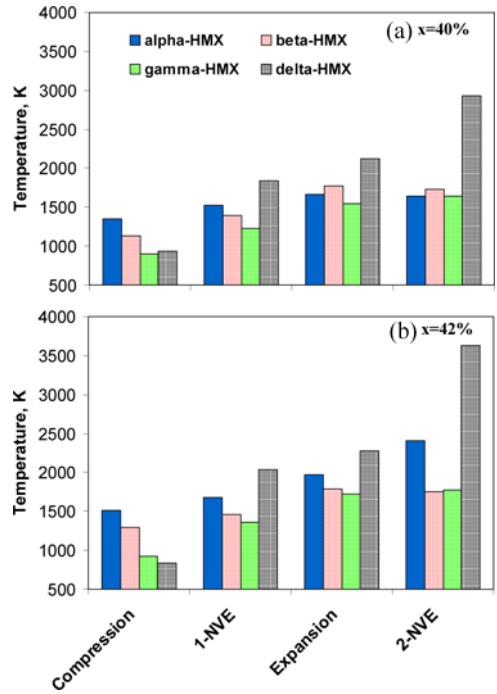

Figure 14. System temperature for the HMX crystals in different phases in the region of compression, first NVE, expansion, and second NVE at the compression ratios (a) $x = 40\%$ and (b) $x = 42\%$.

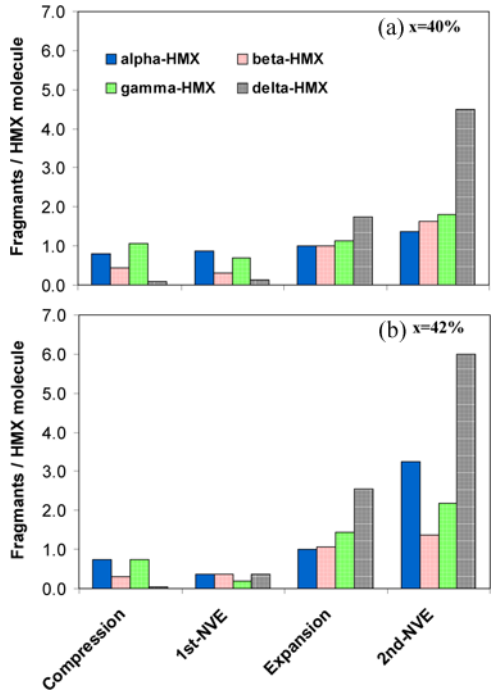

Figure 15. The number of fragments per HMX molecules in the region of compression, first NVE, expansion, and second NVE at the compression ratios (a) $x = 40\%$ and (b) $x = 42\%$.

than δ-HMX but more sensitive than α-HMX and β-HMX. At higher compression ratio $x = 42$, the fragment data show that γ-HMX keeps the same sensitivity order as the one at $x = 40\%$ until the expansion is finished ($\sim$2.1 ps; see Figs. 11b and 15b). Based on the number of fragments per HMX molecule (degree of decomposition) and the temperature changes in the region of compression, first NVE, expansion, and second NVE from the simulation results, the sensitivity of HMX crystals at four phases increases in this order: $\beta < \alpha < \gamma < \delta$. This order is consistent with the experiment by McCrone [46]. More evidence of this stability order will be shown in the following species analysis.

Similar to the individual species analysis of RDX, Figs. 12a–12f compare the individual species of HMX, others, NO_2, NO, HONO, and H_2O, respectively, for α-HMX, β-HMX, γ-HMX, and δ-HMX. For the species HMX, Fig. 12a shows that in the δ-phase all HMX molecules decompose very quickly and generate many intermediates and final products, as identified in those cases of RDX, whereas in α-, β-, and γ-phases HMX molecules are clustered during compression and then fewer HMX molecules decompose to generate just a few intermediates such as NO_2, NO, and HONO. Similar species from the decomposition of HMX have been found by experiments [48]. The total number of these individual species is less than 0.1 per HMX molecule, as shown in Figs. 12c–12e. Figure 12b shows the comparison of the others for these four phases. For these cases of HMX, the others are defined as the summation of those fragments whose maximal occurrence is less than 2 in the whole simulation process. As can be seen, many more new fragments are generated from δ-HMX than from the other three phases. The individual species analysis in Fig. 12 also confirms that the sensitivity of HMX crystals at four phases increases in this order: $\beta < \alpha < \gamma < \delta$.

Because all HMX molecules decompose and generate many intermediates and further final products, a detailed species analysis was performed for the cases of δ-HMX at the compression ratios of $x = 40$ and 42%, as shown in Fig. 16 (for clarity the lines for those species whose total number is less than 2 are removed). In these cases of δ-HMX at $x = 40$ and 42%, intermediates NO_2, NO, OH, and HONO and final products H_2O, N_2, CO, CO_2, and O_2 are found from the decomposition. At a later stage of the decomposition process (>4.8 ps), the number of intermediates NO_2, NO, and OH decreases, whereas the number of final products H_2O, N_2, CO increases quickly, indicating that the secondary reactions occur during that time. The intermediates NO_2, NO, OH, and HONO are formed at a very similar time at both compression ratios $x = 40$ and 42%, but evolutions of these intermediates are very different. For example, the number of HONO keep increasing at $x = 40\%$, whereas at $x = 42\%$ it increases in early time ($t < 3.0$ ps) and

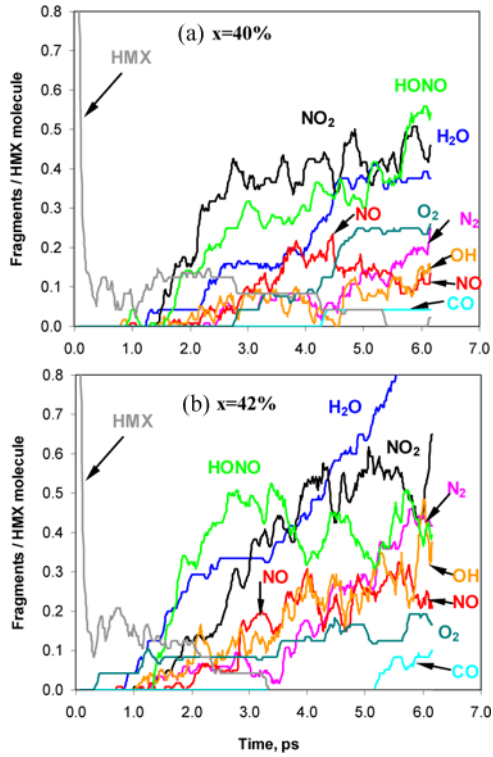

Figure 16. A detailed species analysis for δ-HMX crystal at the compression ratios of (a) $x = 40\%$ and (b) $x = 42\%$.

then keeps decreasing during the rest of the simulation time. Moreover, the final products H_2O, N_2, and CO at $x = 42\%$ are greater than at $x = 40\%$.

From the species analysis above we can conclude that for the cases of α-, β-, and γ-phases all HMX molecules start to decompose and chemical reactions are primary, whereas both primary and secondary reactions are observed for the case of the δ-phase and many more secondary reaction species are produced in this case. The finding from the case δ-phase is very similar to that observed in Fig. 9 for RDX at $x = 42$ and 45% compression ratios. For a better view of the system after the decomposition process,

the final configurations can be seen in Figs. 13a–13d for HMX crystals in the α-, β-, γ-, and δ-phases at $x = 40\%$. For α-HMX and β-HMX, the degree of decomposition is much less than that of δ-HMX. For γ-HMX, it seems greater than those of HMX in α- and β-phases but is certainly less than that of δ-HMX.

In order to explain the sensitivity difference between β- and δ-HMX, we calculated the strain energies of all NO_2 groups in HMX molecules and other atoms (rings in HMX molecules). Figures 17a–17d plot the distributions of strain energy of these NO_2 groups in HMX molecules during the compression region (<0.14 ps) for both β- and δ-HMX. It shows that during

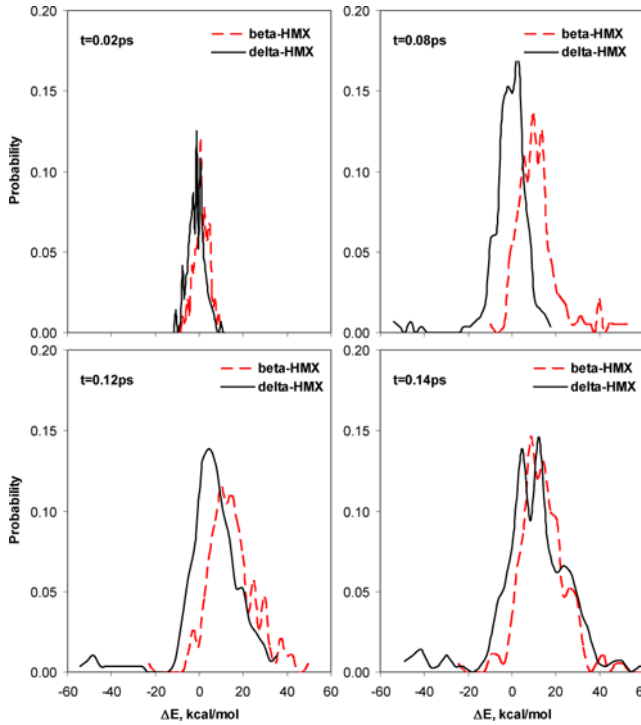

Figure 17. Strain energy distributions for NO_2 groups in HMX molecules for β-HMX (broken lines) and δ-HMX (solid lines) during compression with $x = 42\%$ ($t = 0.02$, 0.08, 0.12, and 0.14 ps).

compression the strain energies of NO_2 group are more widely distributed in δ-HMX than those in β-HMX, particularly at the later compressions $t = 0.12$ and 0.14 ps (Figs. 17c and 17d). We also calculated the area under the curve for the strain energy distribution of groups NO_2 and rings in HMX molecules, as shown in Fig. 18a (NO_2 groups) and Fig. 18b (ring groups). For ring groups, integrated areas under the curve between β- and δ-HMX have no big difference. For NO_2 groups, at the beginning of the compression ($t < 0.04$ ps), the integrated areas under the curve are very similar in both β- and δ-HMX, whereas the areas under the curve at later compressions ($0.04 \text{ ps} < t < 0.14 \text{ ps}$) in δ-HMX are always larger than those in β-HMX, indicating that more strain energy is stored in the NO_2 group for δ-HMX during the compression. These strain

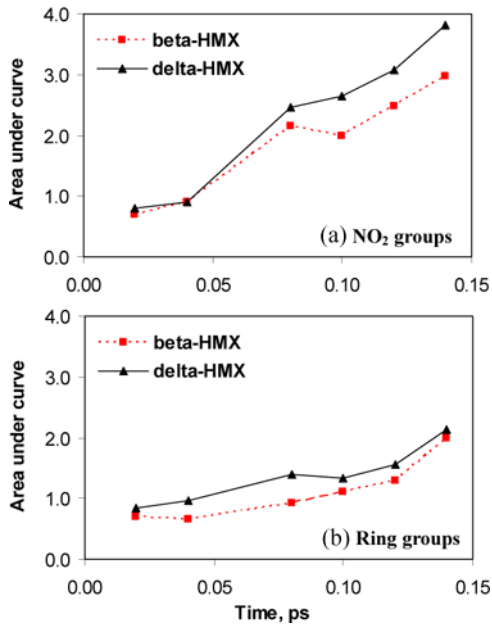

Figure 18. Integrated areas under the curve of strain energy distribution for (a) NO_2 and (b) ring groups in HMX molecules for β-HMX (broken lines) and δ-HMX (solid lines) during compression with $x = 42\%$.

energies result in a breakage of the NO_2 group from HMX molecules, which has been suggested as an initial step by experiments and QM calculations [44,48–50]. The potential energy calculations suggest that the differences in strain energy buildup observed at the fast compression stage in our simulations could be related to the variation of sensitivity of different HMX phases.

Conclusions

In this work, we used reactive dynamic simulations with the ReaxFF force field to model the impact sensitivity of RDX and of four HMX phases (α, β, γ, and δ) at various compression ratios by a high rate compression–expansion approach. For the RDX crystals, at lower compression ratios ($x < 40\%$) only a few RDX molecules decompose and only primary reactions are found during this decomposition process, which produces a few intermediates; for example, NO_2, NO, HONO. At higher compression ratios ($x > 40\%$), all RDX molecules decompose very quickly and both primary and secondary reactions are found in the decomposition processes, which produce not only various intermediates but also the final products H_2O, N_2, CO, CO_2, which have been identified by many experimental measurements [48]. The simulation results suggest that the critical compression ratio for RDX is about 40% in volume at a rate of 8.76 km/s. For the HMX in different phases, it is shown that the impact sensitivity increases in this order: $\beta < \alpha < \gamma < \delta$. At the same compression ratio $x = 40\%$, all HMX molecules in the δ-phase decompose quickly and both primary and secondary reactions are found. However, only a few HMX molecules in α-, β-, and γ-phases decompose. At a higher compression ratio ($x = 42\%$), secondary reactions start earlier and more find products are formed. The results for HMX crystals in four phases are in agreement with those obtained from experiments [44]. Analysis of the simulation results suggests that the strain energy stored in NO_2 groups in HMX molecules during the compression is responsible for the sensitivity difference for HMX crystals.

This study has demonstrated that the high rate compression–expansion approach by RD simulations with the ReaxFF force field can be used to evaluate the sensitivity of RDX and HMX high explosives. We are currently using this approach equipped with the ReaxFF to test other energetic materials (e.g., pentaerythritol tetranitrate and triamino trinitrobenzene). Typically, CPU time for one simulation run (up to 45% compression) is between 10 and 24 h on a single 3.0-GHz processor, but most simulations require less than 18 h of CPU time. The RD simulation approach proposed in this work provides a tool for fast evaluation of the sensitivity and coupling between mechanical impact and reactivity of energetic materials.

References

[1] Cooper, P. W. 1996. *Explosive Engineering*. New York: Wiley-VCH.

[2] Yoh, J. J., M. A. McCleland, J. L. Maienschein, and F. F. Wardell. 2005. Towards a predictive thermal explosion model for energetic materials. *Journal of Computer-Aided Materials Design*, 10: 175.

[3] Agrawal, J. P. 1998. Recent trends in high-energy materials. *Progress in Energy and Combustion Science*, 24: 1.

[4] Balzer, J. E., W. G. Proud, S. M. Walley, and J. E. Field. 2003. High-speed photographic study of the drop-weight impact response of RDX/DOS mixtures. *Combustion and Flame*, 135: 547.

[5] Sharma, J., B. C. Beard, and M. Chaykovsky. 1991. Correlation of impact sensitivity with electronic levels and structure of molecules. *Journal of Physical Chemistry*, 95: 1209.

[6] Brenner, D. W., D. H. Robertson, M. L. Elert, and C. T. White. 1993. Detonations at nanometer resolution using molecular dynamics. *Physical Review Letters*, 70: 2174.

[7] Edward, J., C. Eybl, and B. Johnson. 2004. Correlation between sensitivity and approximated heats of detonation of several nitroamines using quantum mechanical methods. *International Journal of Quantum Chemistry*, 100: 713.

[8] Gruzdkov, Y. A. and Y. M. Gupta. 2000. Shock wave initiation of pentaerythritol tetranitrate single crystals: Mechanism of

anisotropic sensitivity. *Journal of Physical Chemistry A*, 104: 11169.

[9] Wu, C. J. and L. E. Fried. 1997. Ab initio study of RDX decomposition mechanisms. *Journal of Physical Chemistry A*, 101: 8675.

[10] Nefati, H., J.-M. Cense, and J.-J. Legendre. 1996. Prediction of the Impact Sensitivity by Neural Networks. *Journal of Chemical Information and Computer Sciences*, 36: 804.

[11] Vaullerin, M. and A. Espagnacq. 1998. Prediction of explosives impact sensitivity. *Propellants, Explosives, Pyrotechnics*, 23: 237.

[12] Dubovik, A. V. 2002. Model of impact initiation of composite explosive solid systems. *Combustion, Explosion, and Shock Waves*, 38: 714.

[13] Chidester, S. K., C. M. Tarver, L. G. Green, and P. A. Urtiew. 1997. On the violence of thermal explosion in solid explosives. *Combustion and Flame*, 110: 264.

[14] Kamlet, M. J. and H. G. Adolph. 1981. Some comments regarding the sensentivities, thermal stabilities, and explosive performance characteristics of fluorodinitromethyl compounds. In *Proceedings of the 7th Symposium (International) on Detonation*. Annapolis, Marland.

[15] Mullay, J. A. 1987. A relationship between impact sensitivity and molecular electronegativity. *Propellants, Explosives, Pyrotechnics*, 12: 60.

[16] Mullay, J. 1987. Relationships between impact sensitivity and molecular electronic structure. *Propellants, Explosives, Pyrotechnics*, 12: 121.

[17] Mullay, J. 1984. Atomic and group electronegativities. *Journal of the American Chemical Society*, 106: 5842.

[18] Mullay, J. 1985. Cation binding effect on hydrogen bonding. *Journal of the American Chemical Society*, 107: 7271.

[19] Mullay, J. 1986. A simple method for calculating atomic charge in molecules. *Journal of the American Chemical Society*, 108: 1770.

[20] Kohno, Y., K. Maekawa, T. Tsuchioka, T. Hashizume, and A. Imamura. 1994. A relationship between the impact sensitivity and the electronic structures for the unique N−N bond in the HMX polymorphs. *Combustion and Flame*, 96: 343.

[21] Politzer, P., J. M. Seminario, and P. R. Bolduc. 1989. A proposed interpretation of the destabilizing effect of hydroxyl

groups on nitroaromatic molecules. *Chemical Physics Letters*, 158: 463.

[22] Murray, J. S., P. Lane, P. Politzer, and P. R. Bolduc. 1990. A relationship between impact sensitivity and the electrostatic potentials at the midpoints of C−NO_2 bonds in nitroaromatics. *Chemical Physics Letters*, 168: 135.

[23] Politzer, P., J. S. Murray, P. Lane, P. Sjoberg, and H. G. Adolph. 1991. Shock-sensitivity relationships for nitramines and nitroaliphatics. *Chemical Physics Letters*, 181: 78.

[24] Delpuech, A. and J. Cherville. 1978. Relation entre la structure electronique et la sensibilité au choc des explosifs secondaires nitrés-critère moléculaire de sensibilité. I. Cas des nitroaromatiques et des nitramines. *Propellants, Explosives, Pyrotechnics*, 3: 169.

[25] Delpuech, A. and J. Cherville. 1979. Relation entre la structure electronique et la Sensibilité au Choc des explosifs secondaires nitrés. Nritère moléculaire de Sensibilité II. Cas des esters nitriques. *Propellants, Explosives, Pyrotechnics*, 4: 121.

[26] Delpuech, A. and J. Cherville. 1979. Relation entre la structure electronique et la sensibilité au choc des explosifs secondaires nitrés. III. Influence de l'environnement cristallin. *Propellants, Explosives, Pyrotechnics*, 4: 61.

[27] Delpuech, A. and J. Cherville. 1981. Molecular electronic structure and initiation of secondary explosives. In *Proceedings of the 7th Symposium (International) on Detonation*. Annapolis, Marland.

[28] Strachan, A., A. C. T. van Duin, D. Chakraborty, S. Dasgupta, and W. A. Goddard, III. 2003. Shock Waves in High-Energy Materials: The Initial Chemical Events in Nitramine RDX. *Physical Review Letters*, 91: 098301.

[29] Strachan, A., E. Kober, A. C. T. van Duin, J. Oxgaard, and W. A. Goddard, III. 2005. Thermal decomposition of RDX from reactive molecular dynamics. *Journal of Chemical Physics*, 122: 054502.

[30] Zhang, L., S. V. Zybin, A. C. T. van Duin, S. Dasgupta, and W. A. Goddard. 2009. Carbon cluster formation during thermal decomposition of octahydro-1,3,5,7-tetranitro-1,3,5,7-tetrazocine and 1,3,5-triamino-2,4,6-trinitrobenzene high explosives from ReaxFF reactive molecular dynamics simulations. *Journal of Physical Chemistry A*, 113: 10619.

[31] Zhang, L., A. C. T. van Duin, S. V. Zybin, and W. A. Goddard. 2009. Thermal decomposition of hydrazines from reactive

dynamics using the ReaxFF reactive force field. *Journal of Physical Chemistry B*, 113: 10770.

[32] Budzien, J., A. P. Thompson, and S. V. Zybin. 2009. Reactive molecular dynamics simulations of shock through a single crystal of pentaerythritol tetranitrate. *Journal of Physical Chemistry B*, 113: 13142.

[33] Zybin, S. V., W. A. Goddard, P. Xu, A. C. T. van Duin, and A. P. Thompson. 2010. Physical mechanism of anisotropic sensitivity in pentaerythritol tetranitrate from compressive-shear reaction dynamics simulations. *Applied Physics Letters*, 96: 081918.

[34] van Duin, A. C. T., S. Dasgupta, F. Lorant, and W. A. Goddard, III. 2001. ReaxFF: A reactive force field for hydrocarbons. *Journal of Physical Chemistry A*, 105: 9396.

[35] van Duin, A. C. T., A. Strachan, S. Stewman, Q. Zhang, X. Xu, and W. A. Goddard, III. 2003. $\text{ReaxFF}_{\text{SiO}}$ reactive force field for silicon and silicon oxide systems. *Journal of Physical Chemistry A*, 107: 3803.

[36] Zhang, Q., T. Cagin, A. C. T. van Duin, W. A. Goddard, III, Y. Qi, and L. Hector. 2004. Adhesion and nonwetting-wetting transition in the Al/α-Al_2O_3 interface. *Physical Review B*, 69: 045423.

[37] Nielson, K., A. C. T. van Duin, J. Oxgaard, W. Deng, and W. A. Goddard III. 2005. Development of the ReaxFF reactive force field for describing transition metal catalyzed reactions, with application to the initial stages of the catalytic formation of carbon nanotubes. *Journal of Physical Chemistry A*, 109: 493.

[38] Cheung, S., W. Deng, A. C. T. van Duin, and W. A. Goddard, III. 2005. $\text{ReaxFF}_{\text{MgH}}$ reactive force field for magnesium hydride systems. *Journal of Physical Chemistry A*, 109: 851.

[39] Armstrong, R. W. 1995. Dislocation mechanisms for shock-induced hot spots. *Journal de Physique IV*, Colloqoques, 5: 89.

[40] Armstrong, R. W., H. L. Ammon, Z. Y. Du, W. L. Elban, and X. J. Zhang. 1993. Energetic crystal-lattice-dependent responses. *Materials Research Society Symposium Proceedings*, 296: 227.

[41] Maillet, J.-B., M. Mareschal, L. Soulard, R. Ravelo, P. S. Lomdahl, T. C. Germann, and B. L. Holian. 2001. Uniaxial Hugoniostat: A method for atomistic simulations of shocked materials. *Physical Review E*, 63: 016121.

[42] Reed, E. J., L. E. Fried, and J. D. Joannopoulos. 2003. A method for tractable dynamical studies of single and double shock compression. *Physical Review Letters*, 90: 235503.

[43] Allen, M. P. and D. J. Tildesley. 1987. *Computer Simulation of Liquids*. Oxford: Clarendon.

[44] (a) Behrens, R. Jr., and S. Bulusu. 1991. Thermal decomposition of energetic materials. 2. Deuterium isotope effects and isotopic scrambling in condensed-phase decomposition of octahydro-1,3,5,7-tetranitro-1,3,5,7-tetrazocine. *Journal of Physical Chemistry*, 95: 5838; (b) Behrens, R. Jr., and S. Bulusu. 1992. Thermal decomposition of energetic materials. 4. Deuterium isotope effects and isotopic scrambling (H/D, 13C/18O, 14 N/15 N) in condensed-phase decomposition of 1,3,5-trinitrohexahydro-s-triazine (RDX). *Journal of Physical Chemistry*, 96: 8891.

[45] Brill, T. B., P. E. Gongwer, and G. K. Williams. 1994. Thermal decomposition of energetic materials. 66. Kinetic compensation effects in HMX, RDX, and NTO. *Journal of Physical Chemistry*, 98: 12242.

[46] McCrone, W. C. 1965. Physics and chemistry of the solid state. In D. Fox, M. M. Labes and A. Weissberger (eds.), *Physics and Chemistry of the Organics Solid State*, New York: Wiley.

[47] Cady, H. W. 1962. *Studies on the polymorphs of HMX*. LAMS-2652. Los Alamos National Laboratory.

[48] (a) Behrens, R. Jr. 1990. Thermal decomposition of energetic materials: Temporal behaviors of the rates of formation of the gaseous pyrolysis products from condensed-phase decomposition of octahydro-1,3,5,7-tetranitro-1,3,5,7-tetrazocine. *Journal of Physical Chemistry*, 94: 6706; (b) Behrens, R. Jr., and S. Bulusu. 1992. Thermal decomposition of energetic materials. 3. Temporal behaviors of the rates of formation of the gaseous pyrolysis products from condensed-phase decomposition of 1,3,5-trinitrohexahydro-s-triazine (RDX). *Journal of Physical Chemistry*, 96: 8877.

[49] Lewis, J. P., K. R. Glaesemann, K. VanOpdorp, and G. A. Voth. 2000. Ab initio calculations of reactive pathways for α-octahydro-1,3,5,7-tetranitro-1,3,5,7-tetrazocine (α-HMX). *Journal of Physical Chemistry A*, 104: 11384.

[50] Chakraborty, D., R. P. Muller, S. Dasgupta, and W. A. Goddard, III. 2001. Mechanism for unimolecular decomposition of HMX (1,3,5,7-tetranitro-1,3,5,7-tetrazocine), an ab initio study. *Journal of Physical Chemistry A*, 105: 1302.